AN EXPERIMENTAL AND COMPUTATIONAL STUDY OF THE EFFECT OF NOSE BLUNTING ON A CONICAL NOSED BODY AT TRANSONIC SPEED

S. A. Prince & N. G. Goizueta
City University London, UK
s.a.prince@city.ac.uk

Abstract

This paper presents a small sample of the data so far obtained on an ongoing systematic and detailed investigation of the effect of spherical nose rounding on conical nosed bodies at transonic speed. It can be concluded that modern computational fluid dynamics (CFD) methods are capable of resolving the complicated compressible, viscous flows that occur in these cases. Although more data is needed to make firm conclusions, the results so far suggest that:

i) Small levels of spherical nose rounding (radius of less than 40% of the cylindrical afterbody radius) do not significantly increase overall axial force.

ii) The formation of "horn" or "tornado" like vortices on the rounded nose appear to be associated with local laminar flow over the nose.

1 Introduction

The effect of nose bluntness on the flow around a forebody is of particular interest in the area of missile design, where nose mounted seekers tend to require a rounded window through which they can have an undistorted view of the target. Nose bluntness has a number of aerodynamic implications, not least a general increase in the aerodynamic axial force (drag at zero angle of attack).

At moderate to high angles of attack, α, on a blunt nosed body a local Werle-Legendre foci-type boundary layer separation[1,2] can occur whereby the shear layer is funnelled into a spiral vortex emerging tangentially out from the surface before turning into the main stream to form longitudinal, horn like, primary vortices.

The nature of this tornado like nose vortex was investigated by Hsieh[3] who studied low supersonic flow over hemisphere-cylinder bodies at angle of attack. Wind tunnel experiments were performed at Mach numbers between 1.1 and 1.5, with angles of attack up to α=19°, and Reynolds numbers between 5.0 - 5.4x10^6 per foot. Figures 1 and 2 present a summary of Hsieh's results. At low to moderate incidence two flow separation regions can often be observed. Separation type I is the usual crossflow separation seen with sharp nosed bodies that results in the formation of leeside longitudinal vortex pairs. Separation type II, which is common to blunt nosed bodies, is a leeside separation bubble which forms because of the strong adverse pressure gradient resulting from nose bluntness and incidence.

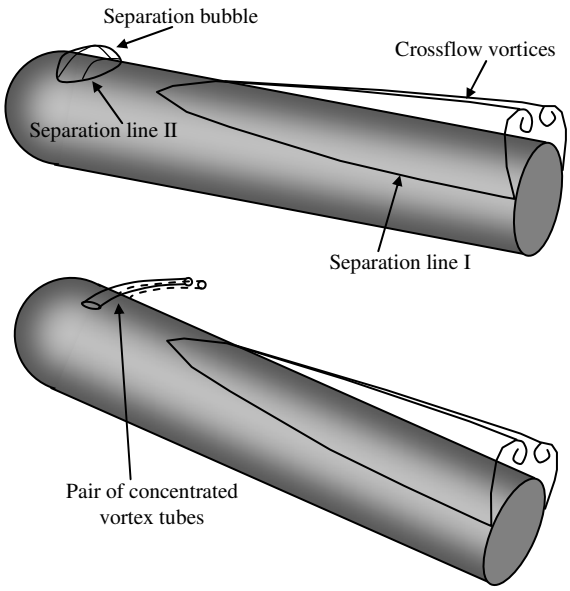

Fig 1: Variation of flow topology with angle of attack for a hemispherical nosed body according to Hsieh.

Hseih found that the leeside separation bubble of separation type II tended not to occur at angles of attack of less than 10°, though this is certainly highly Reynolds number dependent. As shown in figure 1, Hsieh observed that at moderate angles of attack both separation types I and II can coexist, with type I separation resulting in a closed bubble with a reattachment line.

As the angle of attack increases, the bubble size grows, extending further downstream until the bubble breaks down. At α=19°, for both M=1.2 and 1.4, Hsieh found that a Werle-Legrandre separation occurred with the formation of a concentrated vortex pair, reminiscent of horns, emanating from the leeside of the nose, as shown in figure 1. At even higher angle of attack the separation lines I and II merge together and the Werle-Legrandre vortices disappear. Figure 2 presents a summary of the surface skin friction patterns that were seen to develop in Hsieh's experiments as angle of attack was increased, corresponding to the flow topologies shown in figure 1.

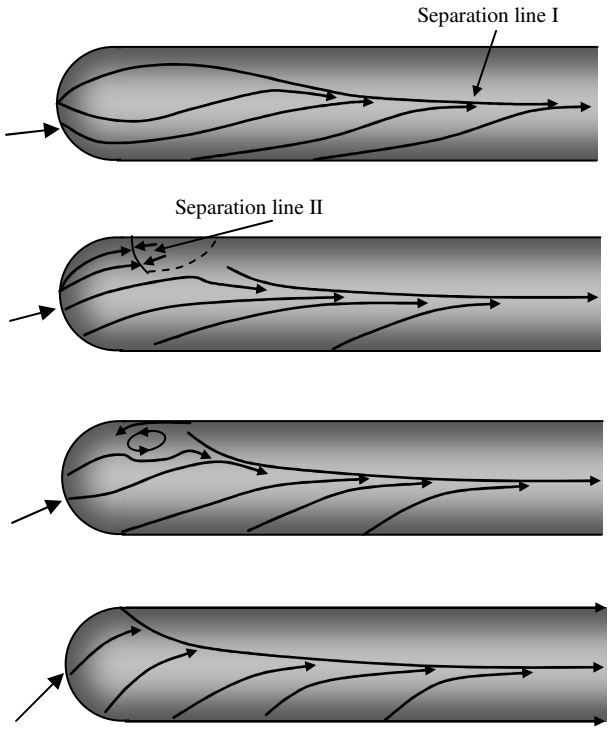

Fig 2:Variation of surface skin friction lines on a hemispherical nosed body with increasing angle of attack according to Hsieh

In addition to the complicated separated flows that can develop for blunted nosed bodies, another interesting effect of nose blunting has been found to be a drag reduction, for some levels of rounding radius, compared with the corresponding sharp nosed body flow. This, rather counterintuitive result, has been reported by a number of investigators[4-6].

Ward[4] performed an experimental study of the aerodynamic characteristics of a class of blunted nosed circular cross-section bodies at transonic and supersonic speed ($0.4 < M < 2.0$) with varying nose rounding and nose fineness ratio. The study encompassed ten different nose profiles. In particular, the study included the measurement of the variation of axial force with Mach number for the case of zero degrees angle of attack. Interestingly, the data shows that a small nose rounding diameter of 0.3 results in lower axial force than that measured for the corresponding sharp nose. The data also shows that for the sharp nose and for nose rounding diameters of less than 0.7, a local maximum in axial force is seen between M=1.1 and 1.3. This feature, however, is not seen for the very bluff bodies.

Similar studies, performed by Wallskog and Hart[6] and Polhamus[5], investigated nose rounding of blunted nosed cylindrical bodies compared with a series of sharp nosed ogival and conical nose shapes. Together, these studies covered the Mach number range $0.4 < M < 2.3$. The measurements indicate that a small nose rounding radius can result in small reductions in axial force compared with the corresponding sharp nosed body.

This paper presents some initial results of a comprehensive study to investigate the effects of nose rounding on the aerodynamics of conical and ogival bodies of revolution at transonic and supersonic speeds. The study aims to provide wind tunnel data as well as CFD data to gain greater insight into the complicated viscous / compressible flows associated with blunted nosed forebodies.

2 Investigation Methodology

The results presented in this paper are for a family of conical nosed D = 28.7mm diameter

bodies presented in figure 3. Model A is a 1.85 calibre sharp nosed cone-cylinder. Models B and C have the same geometry except that their noses were rounded by radius, *r*, of 0.35*R* and 0.70*R* respectively, as shown in figure 3.

Model	r/R	L (mm)	a (mm)	b (mm)	D (mm)
A	0	129.7	76.6	53.1	28.7
B	0.35	115.1	76.6	38.5	28.7
C	0.70	100.7	76.6	24.1	28.7

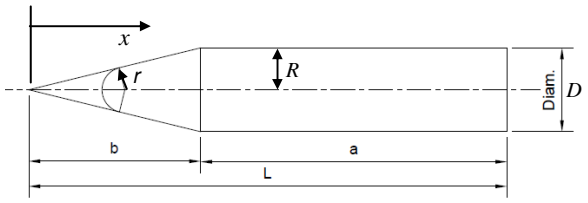

Fig 3: Geometries of the blunted nosed body wind tunnel models.

2.1 Experimental Details

The models were manufactured out of stainless steel with surface pressure tapings made with 0.5mm ID brass tubes accommodated in longitudinal grooves machined along the body length, and finished smooth with epoxy resin. The conical nose has 11 tapings, while the 0.35*R* and 0.70*R* blunted nosed models have 16 and 13 tapings respectively, with one in the centre of the nose.

Experiments were performed in the City University London T5 transonic-supersonic wind tunnel. This intermittent, ejector driven, closed return wind tunnel was operated in transonic mode ($0.7 < M < 1.1$) with slotted wall working section liners and at $M = 1.55$ with contoured nozzle liners. The working section of 250mm x 200mm x 500mm allowed the sting mounted models to be pitched in the angle of attack range $9^o < \alpha < -7^o$. Reynolds number varied in the range (depending on the operating Mach number) 4 – 4.9 million per metre.

Run times of around 30 seconds, with stabilized flow, were possible at transonic speed, while at supersonic speed about 5 – 6 seconds of stabilized flow were achieved with a Mach number repeatability of ±0.1. Surface pressure data was acquired using a 36 channel electronic dynamic pressure scanner, connected to the model via polythene tubes. The model was rotated by increments of 5^o in roll in order to obtain full surface pressure distributions for the angle of attack cases. The accuracy of the pressure transducers for the Mach numbers / pressure levels investigated is estimated at Cp ~ ±0.02.

Data presented in this study include selected surface pressure data and shadowgraph flow visualisation images, although a 5 component strain gauge sting balance will also be employed to measure the forces and moments with angle of attack.

2.2 Computational Simulation Details

The computational simulations of the flow around the three nose geometries is being performed using a commercial Navier-Stokes computational fluid dynamics solver. The solver employs a cell-centred, finite volume method that can be used with structured, unstructured or hybrid grids. The coupled solver, used in this investigation, solves the continuity and momentum equations simultaneously. Temporal discretization of the coupled equations is accomplished by either an implicit or explicit time-marching scheme. The explicit scheme uses a multi-stage Runge-Kutta method, while the implicit scheme uses a Newton-type flux linearization with a point Gauss-Seidel algorithm. The spatial discretization uses an upwind, flux-difference splitting scheme similar to that of Roe.

For this study simulations have been run to match the wind tunnel conditions – constant total pressure and temperature, and varying Mach numbers and angles of attack. Cases have been computed for Mach numbers of 0.8, 1.0, 1.2, 1.55 and 2.0, with angles of attack of 0 to 15^o at increments of 3^o. Each case has been simulated under laminar conditions and using the Spalart-Allmaras, k-ω Shear Stress Transport, and k – ε turbulence models.

Half domain grids (windward symmetry to leeward symmetry flow domains) with a symmetry boundary condition were employed in the study since it was deemed that up to $\alpha=15^o$ the flows would remain symmetric. The grids were all structured with cell clustering towards

the body surface such that the first near wall cell height was set as $1x10^{-5}D$. This generally ensured that the boundary layers were resolved with between 20-30 cells. A grid sensitivity study, performed on six of the highest α cases, revealed that a grid of 730,000 hexahedral cells was sufficient for convergence of force and moment and surface pressure data, once the solution residuals had been reduced by five orders.

3 Results and Discussion

The results presented in this paper are a selection representing a small amount of the experimental and computational data obtained in this study. Section 3.1 presents comparisons between the experimental measurements and the computational predictions for the flows at zero angle of attack, while section 3.2 presents comparisons of the data for the case of 15^o angle of attack at Mach 1.55 ($Re_D = 4 \times 10^5$). The zero angle of attack comparisons aim to prove the accuracy of the computational method, which is used in assessing the physics of blunt body nose separation in section 3.2.

3.1 Zero incidence.

The comparison of experimental shadowgraph image (bottom) with the computed (k-ω SST) density contours (top) is presented for the three nose geometries for zero angle of attack at M = 1.55 in figure 4.

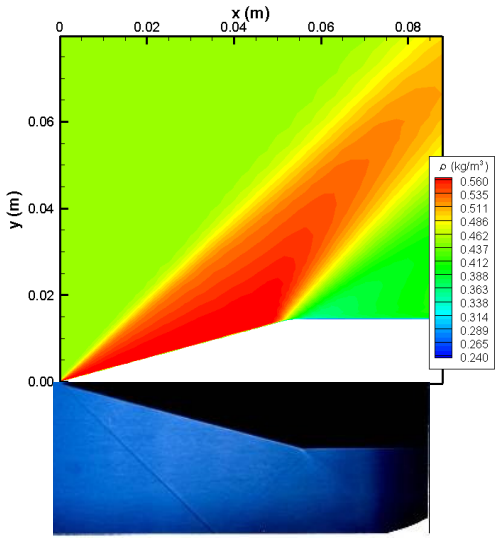

a) Model A (r/R = 0)

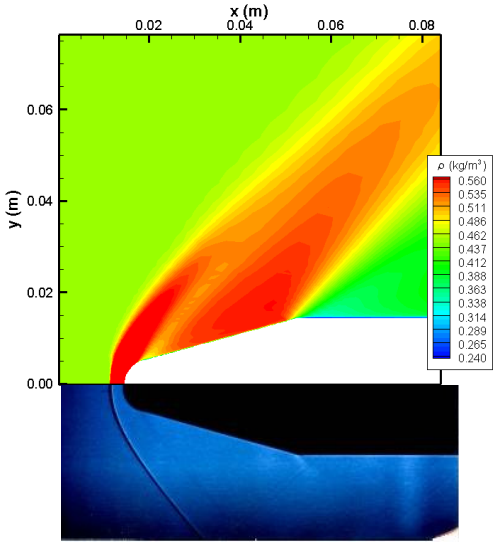

b) Model B (r/R = 0.35)

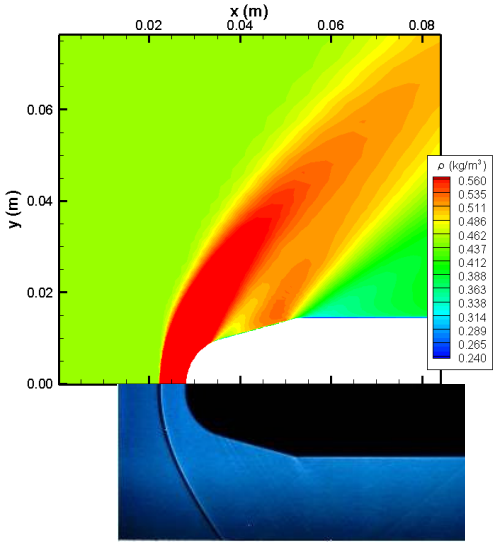

c) Model C (r/R = 0.7)

Fig 4: Comparison of experimental shadowgraph images with CFD predicted (k-ω SST) density contours. M = 1.55, Re_D=4x10^5, α=0^o.

The agreement between the experimentally imaged flow field and that obtained by computational simulation is seen to be remarkably good. In particular the detached shock waves ahead of the blunted nosed bodies is captured with approximately the correct detachment distance and shock shape. The weak shock waves that terminate the supersonic flow region associated with the over-expansion from the spherical portion to the conical surface (these are just visible in the experimental images) are captured very well in the numerical

solutions. No discernable differences were found in the density contours resulting from any of the four computational models at zero angle of attack.

The comparisons of the measured and computed surface pressure distributions for the three geometries are presented in figure 5.

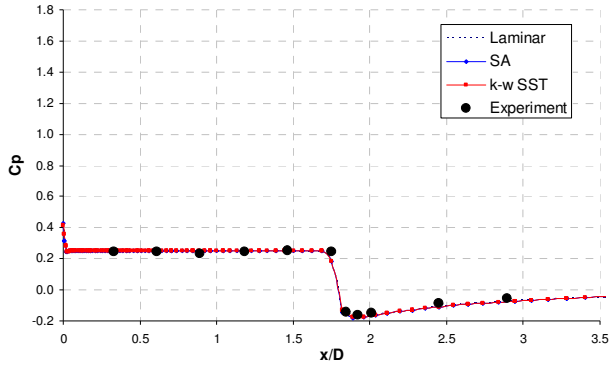

a) Model A (r/R = 0)

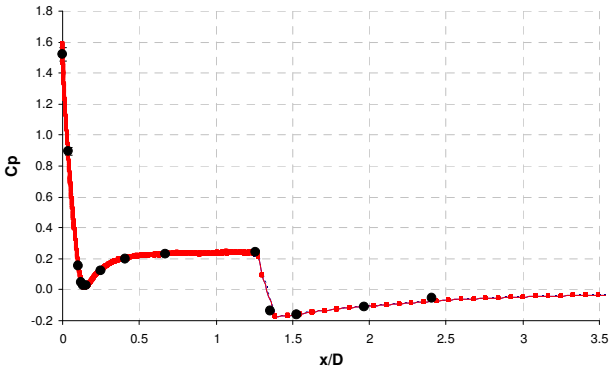

b) Model B (r/R = 0.35)

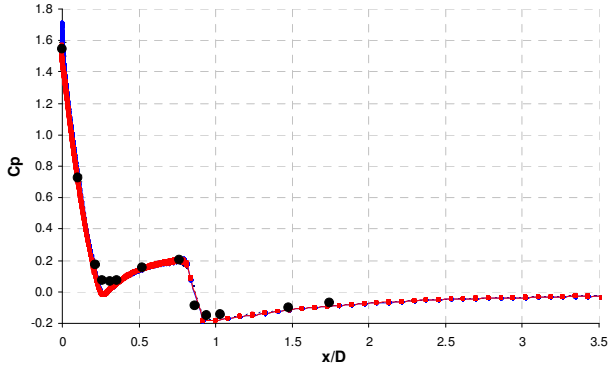

c) Model C (r/R = 0.70)

Fig 5: Surface Cp distributions for the three noses at M=1.55, Re_D=4x10^5, $\alpha = 0^o$.

Again, the agreement between experiment and computation is seen to be very good, with only the expansion onto the conical portion of the nose, perhaps, being over-predicted by the CFD. The *k*-ε turbulence model result is not shown in these plots, as no large differences are seen in any of the other computed pressure differences.

The comparative analysis between the experimental measurements and the computational predictions all verified the validity and accuracy of the computational method for the simulation of the flows at zero angle of attack. CFD solutions were then obtained for all four viscous models across the Mach number range $0.1 < M < 5.0$, with the total pressure and temperature being constant, at the same level as that in the wind tunnel experiments (1.05×10^5 Pa and nominally 288K respectively). Figure 6 compares the predicted axial force variation with Mach number obtained from this series of computations, where both the total force and the pressure contributions are plotted (the skin friction contribution being the difference between the two), with the experimental data available at the time of writing. The experimental values of the pressure contribution to the axial force were obtained by integration of the surface pressure measurements over the body surfaces.

Figure 6 shows only the results for the laminar and the *k*-ω SST calculations for clarity. The Spalart-Allmaras model results gave pressure force data almost equivalent to the *k*-ω SST results, with total axial forces only a few percent higher. The k-ε turbulence model, while also giving almost equivalent pressure force contributions, yielded total axial force predictions up to 15% higher than those predicted using the *k*-ω SST model.

Until experiments using the 5 component sting balance have been completed, no firm conclusions can be made regarding which of the turbulence models gives the best result. However, based on comparisons between CFD and experimental axial force measurements for 2 calibre rounded ogival noses of reference 4 (not presented in this paper) it is suggested that the k-ω SST model gives marginally better predictions than the Spalart-Allmaras model, and that the *k*-ε model is inadequate for this class of flow problem – over-predicting considerably the axial force over the whole Mach number range.

Experiments are also being performed in a low speed wind tunnel in order to provide surface pressure data at M = 0.1 and 0.2, though only the M = 0.1 results for the sharp nosed cone is presented here.

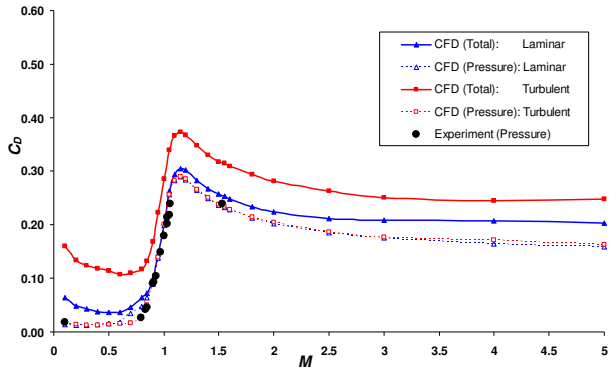

a) Model A (r/R = 0)

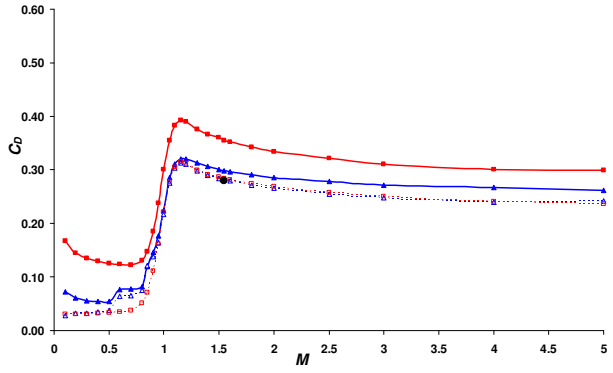

b) Model B (r/R = 0.35)

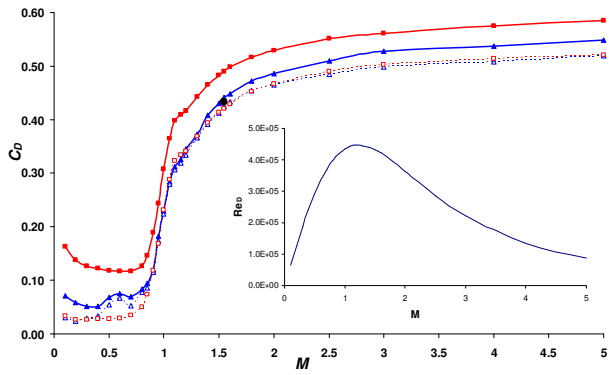

c) Model C (r/R = 0.70)

Fig 6: Variation of zero incidence drag (axial force) coefficient with Mach number, constant stagnation pressure and temperature.

The agreement between the experimentally derived pressure force data and the computed data from the k-ω SST model is seen to be very good, particularly in the range $0.8 < M < 0.95$ where (for the sharp nose model) the laminar predicted pressure forces are over-predicted. The laminar predictions in the high subsonic Mach number range exhibit significant boundary layer separations under the transonic shock waves that are seen to develop over the body. These are not resolved by any of the turbulent predictions – the turbulent boundary layers being sufficiently energetic to survive the adverse pressure gradients, imposed by these relatively weak shocks, without separating. The data presented in figure 6a) suggests that the experimental flow, at least in the Mach number / Reynolds number range (~4×10^5 as seen in the data plotted in figure 6c)) of the experimental data shown, is predominantly turbulent.

The computational data shows that the trend, with Mach number, in axial force coefficient is very similar for the sharp nosed body and that with nose rounding of $r = 0.35R$. For both cases, the drag / axial force rise, associated with the onset of critical condition, begins at around M = 0.8. Also both curves exhibit a pronounced peak, with the peak value of C_D occurring at M = 1.15 – 1.2. The introduction of the smallest level of nose rounding is not seen to impose a significant increase in the axial force at any Mach number – whether laminar or turbulent.

With nose rounding of $r = 0.7R$, however, there is seen to be a significant penalty in axial force in the supersonic Mach number range, due to the very strong detached bow shock wave imposing high pressures over a larger area than in the smaller rounded nose case. The drag rise Mach number, however, appears to have been unaffected by the increased level of nose rounding.

The computational simulations show that there is no axial force reduction effect at any Mach number, by the introduction of nose rounding of $r = 0.35R$. This is not to say that smaller levels of nose rounding will not yield some level of axial force reduction, compared with the sharp nosed body. Further experimental and computational analysis is needed on equivalent conical bodies with smaller levels of nose rounding to reveal whether such reductions in axial force are possible in conical forebodies,

as experimental evidence suggests for ogival forebodies.

3.2 The Effect of Incidence at *M* = 1.55.

This section presents and compares experimental and computational results for the cases of α = 8.6° and 15° at Mach 1.55. In particular the ability of the computational models to accurately capture the smooth surface separations and subsequent leeside vortex development is assessed. The differences in the downstream flows with the introduction of nose rounding is also investigated, as is the occurrence of type II separation as observed by Hsieh with hemispherical noses.

Figure 7 compares the experimentally measured circumferential pressure distributions at three axial stations on Model C (*r/R*=0.70), with the corresponding CFD predictions for laminar, *k*-ω SST and Spalart-Allmaras viscous models. At *x/D* = 0.1 the agreement between the experimental *Cp* measurements and the computed predictions for all three viscous cases is good. All three computed curves exhibit some degree of spurious jaggedness which results from the resolution of the extremely thin boundary layers so close to the stagnation point on the nose (12 cells as opposed to over 30 cells a little further downstream). However the trends are correctly resolved within the estimated accuracy of the experimental measurements.

At *x/D* = 0.35, where the local boundary layers are much better resolved, the trends are captured much more smoothly, and the agreement between experiment and all three viscous simulations is good, with the computational curves correctly resolved within the estimated accuracy of the experimental measurements, though all three viscous models slightly under-predict the pressure recovery on the leeside of the body. At this axial station the CFD solutions all show that there is, as yet, no crossflow boundary layer separation and so, perhaps, there would not be expected to be any significant differences in the pressure distributions between the three viscous cases.

At *x/D* = 1.74, however, CFD reveals that in all three viscous cases crossflow separation has occurred with the development of a significant leeside vortex.

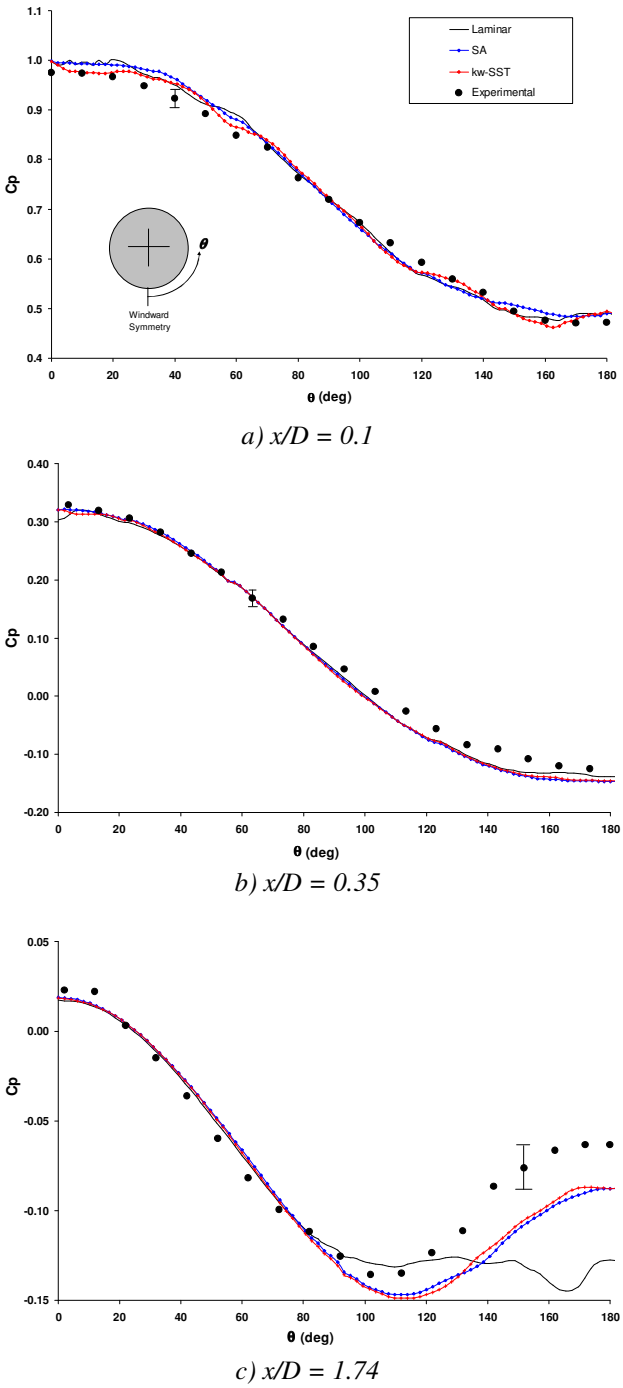

a) x/D = 0.1

b) x/D = 0.35

c) x/D = 1.74

Fig 7: Comparison of experimental and selected CFD computed circumferential surface Cp distributions for the Model C (r/R=0.70), α=8.6°, M=1.52, Re_D=4x10^5.

The laminar solution predicts primary crossflow separation at around ϕ = 70 – 80°, which is far too early when compared with the

experimental data, and the development of an extensive pressure plateau with a suction peak associated with the primary leeside vortex.

Both turbulent curves, which are very similar to each other, agree relatively well with experiment except that they fail to capture the full extent of the pressure recovery seen in the experimental data. This indicates that the experimental flows were almost fully turbulent at Mach 1.55.

The predicted surface pressure contours and associated surface skin friction lines for all three configurations at $\alpha = 15^{o}$ are plotted for Mach 1.55 in figure 8. The results show that the laminar solutions exhibit a much more extensive separated region, arising from the earlier / more upstream occurrence of crossflow separation. Both turbulent calculations gave surface pressure and skin friction patterns in good agreement with each other.

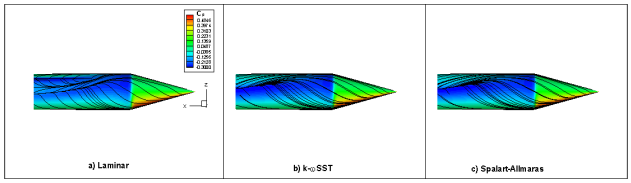

a) Model A (r/R = 0)

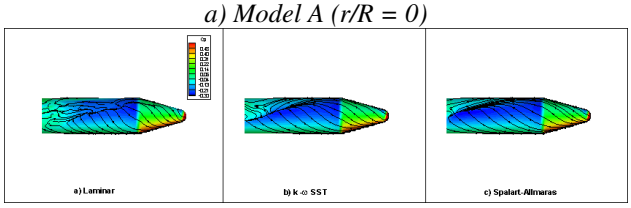

b) Model B (r/R = 0.35)

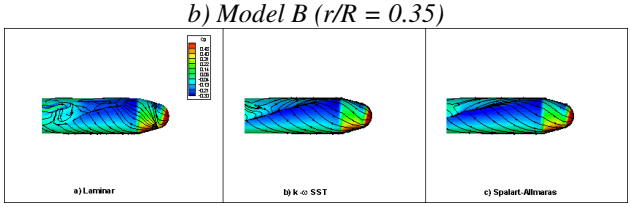

c) Model C (r/R = 0.70)

Fig 8: Computed surface Cp contours and surface skin friction patterns for the three geometries. α=15^{o}, M=1.55, Re_D=4x10^5.

Figure 9 presents the corresponding Mach number contours on the crossflow plane at *x/D* = 1.548. For all three geometries at this axial station, and for all the viscous models, primary crossflow boundary layer separation is resolved with the formation of a leeside primary vortex. While the two turbulent solutions presented, are very similar, in the resolution of a relatively small undeveloped vortex structure and evidence of an embedded crossflow shock wave emanating from close to primary boundary layer separation location, the laminar solutions appear somewhat different. The laminar calculations resolve much more extensive viscous separations, as would be expected, and more developed subsequent vortical features without the appearance of any embedded crossflow shock wave features.

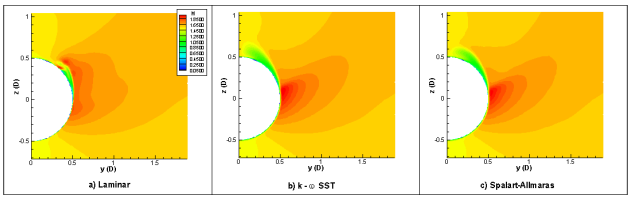

a) Model A (r/R = 0)

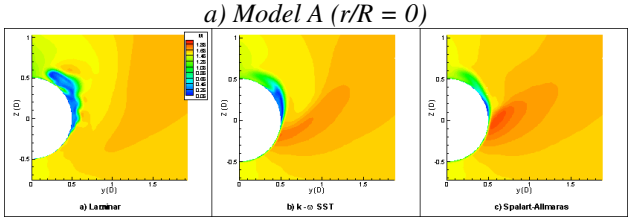

b) Model B (r/R = 0.35)

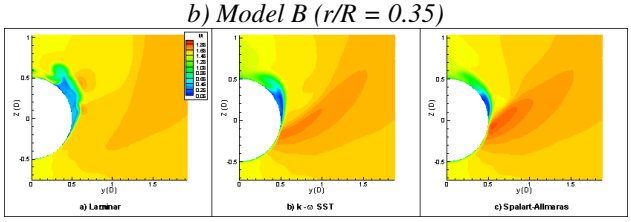

c) Model C (r/R = 0.70)

Fig 9: Computed Mach number contours on crossflow plane at x/D = 1.548 for the three geometries and three viscous cases at α=15^{o}, M=1.55, Re_D=4x10^5.

Close scrutiny of figures 8 and 9 would seem to indicate that the effect of nose rounding is to cause a slightly earlier, more upstream, occurrence of incipient crossflow boundary layer separation. This means that, at any given axial station on the cylindrical afterbody, the extent of viscous separated flow is slightly greater for the rounded nose cases than for the sharp nosed case.

Figures 10 and 11 present the close-up view of the surface skin friction lines for the two rounded nose cases for the laminar and the *k*-ω SST turbulence cases, together with contours of total pressure in the near wall region at a number of axial stations. What this shows is that both laminar flow solutions have captured a

type I separation and the resolution of a small "horn" like vortex of the type observed by Hsieh on hemispherical noses, and by Werle and Legrandre on blunt nosed forebodies.

The corresponding turbulent flows do not, however, exhibit any type I separations or subsequent vortex formation on the nose, the streamlines appearing to develop much more smoothly.

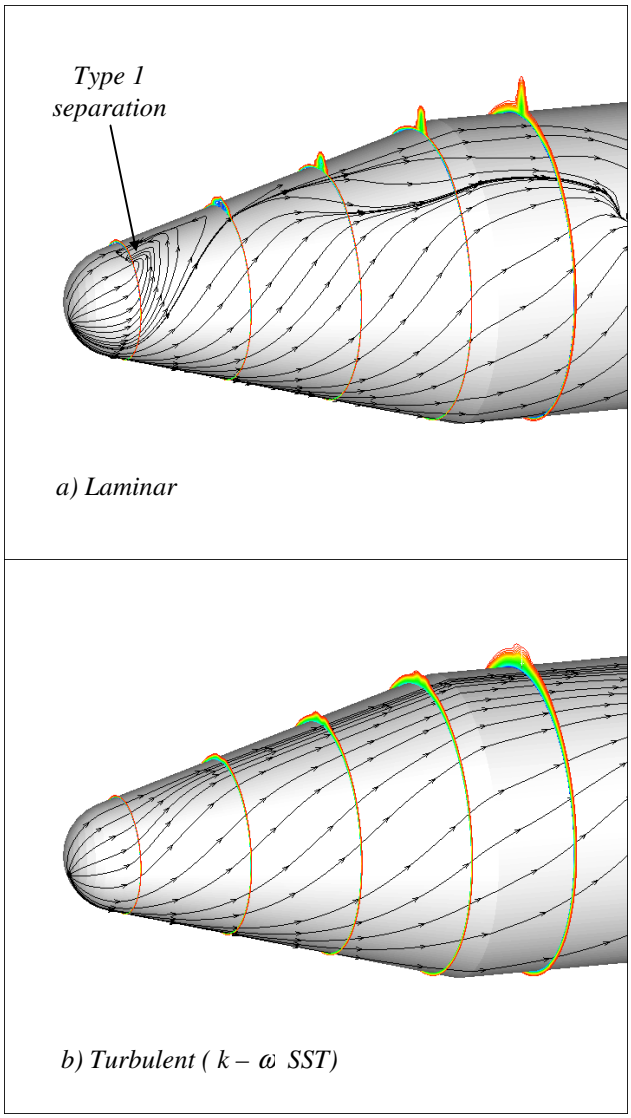

Fig 10: Surface skin friction patterns and selected near-wall total pressure contours for the Mach 1.55 flow around Model B (r/R=0.35) at α=15^o, Re_D=4x10^5.

The CFD calculations for all the other Mach number and angle of attack cases, undertaken in this study, should reveal whether this trend is a general one, and that such type I separations and the associated "tornado" or "horn" like vortices occur when the flow over a rounded nose is laminar. Such features could therefore form in a natural transitional flow where laminar boundary layers are able to extend some distance downstream from the stagnation point.

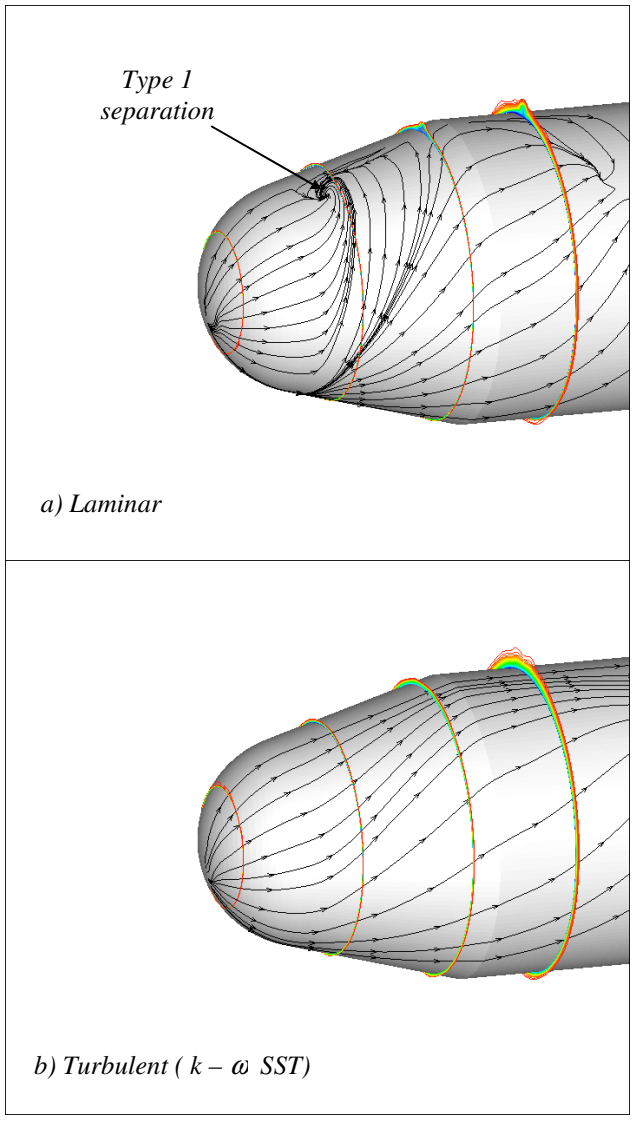

Fig 11: Surface skin friction patterns and selected near-wall total pressure contours for the Mach 1.55 flow around Model C (r/R=0.70) at α=15^o, Re_D=4x10^5.

4 Conclusions.

Though the results presented in this paper represent a small sample of the data so far

obtained in an ongoing systematic and detailed investigation of the effect of nose rounding on conical nosed bodies at transonic speeds, it can be concluded that modern computational fluid dynamics methods are capable of resolving the complicated compressible, viscous flows that occur in these cases.

The data presented so far does not reveal any axial force (drag) reduction effect caused by spherical nose rounding of the sharp nosed conical body investigated in this study, though it is not suggested that such an effect cannot occur with smaller levels of nose rounding. If such an effect exists, it is likely to be resolved in the later calculations due to be undertaken.

While more data is also required to properly assess the conditions at which the type I boundary layer separations occur, and the subsequent formation of the associated "horn" or "tornado" like vortices, it currently seems that the state of the boundary layer over the rounded portion of the nose is a critical factor.

This is important in that type I separations need to be avoided in cases where the rounded nose is used as a window for an Infra-red seeker, where local heating due to boundary layer separations can lead to severe image distortions.

References

[1] Werle, H. "*Separation on Axisymmetrical Bodies at Low Speed*", ONERA Recherche. Aeronautique. No. 90, pp 361-382, 1962.

[2] Legrendre, R. "*Lignes de Courant d'un Ecoulement Continu*", ONERA Recherche. Aeronautique. No. 105, pp. 3-9. 1965.

[3] Hsieh, T. "Low supersonic flow over hemisphere-cylinder at incidence", AIAA Journal of Spacecraft & Rockets, Vol. 14., No. 11, pp662-668. Nov. 1977.

[4] Ward, L. C. "*Force measurements on ten axisymmetric forebodies showing the effects of nose blunting at transonic and supersonic Mach numbers*", RAE TR 78093, August 1978.

[5] Wallskog, H. A. & Hart, R. "*Investigation of the Drag of Blunt-Nosed Bodies of Revolution in Free Flight Mach Numbers from 0.6 to 2.3*" NACA RM L53D14a, June 1953.

[6] Polhamus, Edward C. "*Effect of Nose Shape on Subsonic Aerodynamic Characteristics of a Body of Revolution Having a Fineness Ratio of l0.94*" NACA RM L57F25. August 1957.

Copyright Statement